

POLITECNICO DI TORINO

MASTER DEGREE THESIS

Department of Control and Computer Engineering

Mechatronic Engineering

a.y. 2023/2024



**Politecnico
di Torino**

Study of flexible PCB coils in haptic applications

Supervisors:

Alessandro RIZZO
(*Politecnico di Torino - DET*)

Domenico PRATTICHIZZO
(*Università di Siena - DIISM - SIRSLab*)

Leonardo FRANCO
(*Università di Siena - DIISM - SIRSLab*)

Candidate:

Morgan CASALE

May 2024

POLITECNICO DI TORINO

Abstract

Department of Control and Computer Engineering
Mechatronic Engineering

Study of flexible PCB coils in haptic applications

by Morgan CASALE

As the number of in-orbit satellites increases, the need for a way to service them becomes increasingly critical.

Recently the EU funded EROSS, a project with the purpose of providing a new range of services for in orbit satellites with consequent analysis for satellite design and life-cycle management. This initiative aims to enhance the availability of cost-effective and secure orbital services by assessing and validating the essential technological components of the Servicer spacecraft. The incorporation of robotic space technologies working on this project will lead to greater autonomy and safety in executing these services in space, requiring reduced ground-based supervision.

This master's thesis presents an innovative approach to pose estimation using deep learning and computer vision techniques. The research explores the development and implementation of a system for in-orbit satellites pose estimation. Delving into the complexities of rendezvous maneuvers, the system devised herein addresses the challenges associated with achieving and maintaining accurate pose estimations in the ever-changing and demanding conditions of space. Through a comprehensive exploration, this thesis contributes valuable insights and practical solutions to enhance the reliability and efficiency of satellite rendezvous processes.

A mono camera system is employed, reducing the hardware complexity and costs while maintaining performance. The camera captures pictures of the target satellite during the whole approach phase. A deep learning framework, based on a Convolutional Neural Network (CNN), is used to identify and track landmark features on the target satellite from captured images. This CNN-based approach provides high accuracy in feature recognition and tracking precision. A neural network-based regression model is introduced to map the 2D image coordinates of identified landmarks to their corresponding 3D coordinates with respect to the camera frame. This implementation permits to have a mono-camera instead of a stereo-camera system. Finally, incorporating the CPD algorithm, the system aligns the predicted 3D point clouds to the reference model, enabling accurate pose estimation and tracking.

The proposed system is tested through simulations. The results demonstrate the system's capability to estimate the pose of in-orbit satellites. This research contributes to the advancement of autonomous satellite operations, space debris management, and space exploration. Furthermore, it has the potential to enhance satellite rendezvous and capture capabilities.

Contents

Abstract	i
1 Introduction	1
1.1 Thesis objective	1
1.2 Necessary background (?)	2
1.3 Thesis structure	2
2 Background	4
2.1 Magnetic Coils	4
2.1.1 Brief History	4
2.1.2 Physics of an inductor?	4
Inductance	4
Reactance	5
Joule heating	6
Definition of Root Mean Square (RMS) values	6
2.1.3 Magnetic field generation	6
Magnetic Flux and Field relation	8
2.2 PCB Coils	8
2.2.1 Planar coils	8
2.2.2 Planar coil magnetic field	9
2.2.3 Multi-layer PCB coils	10
Total inductance	11
Magnetic field generated by a Multilayer coil	12
2.3 Flexible PCB coils	12
2.3.1 Pros of flexible coils	12
2.3.2 Application challenges	13
Rise of high resistance	13
Joule effect	14
Magnetic field strength	15
Resistance parasitic effects due to AC current	16
2.3.3 Running flexible PCB coils	19
High current needs	19
Constant Voltage vs Constant Current power supplying	19
2.4 Modelling of the Entire System	20
2.4.1 Neodymium magnets (magnetic strength wrt class and dimensions)	20
2.4.2 Magnetic force between magnet and coil	21
2.4.3 Membrane-magnet system	22
Membrane stiffness	23
Membrane damping	25
2.4.4 Finger grasping model	25

3	Overview of Haptic Feedback	27
3.1	Physics of Haptic Feedback	27
3.1.1	Biology of Haptic Sensing	27
3.1.2	Haptic sensitivity	28
3.2	State of the Art in vibrotactile haptic feedback	29
3.2.1	Piezoelectric actuators	29
	Frequency response	29
	Force performances	30
	Power consumption	30
3.2.2	Texture rendering	30
4	Powering circuit design	31
4.1	Power Circuit Block diagram	31
4.2	Controller	31
4.2.1	ESP32 DAC Characteristics	32
4.2.2	ESP32 waveform generator	32
4.3	Signal Conditioning Circuit	32
4.4	Amplifier circuit	33
4.4.1	Power Operational Amplifiers	33
	Power op-amp characteristics	34
	Power dissipation problems	34
4.4.2	High Power Voltage Amplifier	34
4.4.3	Noise filtering	35
5	Implementation and Prototypes	37
5.1	Coils alternatives	37
5.1.1	Dresda coils	37
	Low magnetic field strenght	37
	Fragility and low flexibility	37
	Very high resistance and power needs	37
5.1.2	Flexar coils	37
	Higher magnetic field strenght	37
	Higher flexibility	37
	Lower resistance and power needs	37
5.2	Rigid Prototypes	37
5.2.1	1st version - Dresda Coils testbed	37
	Dresda Coils	38
	Flexible magnetic membrane	38
	Adjustable height platform for coil and membrane	38
5.2.2	Wearable Rigid Prototypes	38
	Finger-Membrane interface	38
	Keep the distance from the coil	38
	Heat dissipation	38
5.3	Flexible Mat Prototypes	39
5.3.1	Design of the membrane	39
	Material stiffness and thickness	39
	Membrane structure vs magnet dimensions	39
5.3.2	Design of the mat	39
	Distance magnet-coil	39
	Coil trap	39
	Production method and structure	39

5.3.3	Design faults and problems	39
	Membrane fragility	39
	Overall system flexibility	39
	Keeping the distance coil-magnet under finger pressure	39
	Production method	39
5.4	Experimentation and Evaluation	39
5.4.1	Heating testing	39
	Single coil in DC	39
	Single coil in AC [-V, V]	39
	Single coil in AC [0, V]	39
	Two coils in parallel DC	39
	Two coils in parallel AC	39
5.4.2	Magnet size vs Force	39
5.4.3	Force vs number of coils	39
5.4.4	Voltage vs Force	39
6	Discussion and conclusions	40
6.1	Challenges in On-Board AI Systems for Space Missions	40
6.1.1	Verifiability Issues	40
6.1.2	Computational Issues	40
6.2	Results Analysis	41
6.3	Possible Improvements	41
6.3.1	Landmark Mapping Sensitivity	41
6.4	Conclusions	42
A	Support Code	43
A.1	Ground Truth Heatmaps	43
A.2	Landmark Location Selection	44
	Bibliography	45
	Acknowledgements	46

List of Figures

2.1	RMS values for different waveforms.	7
2.2	Magnetic field generated by a solenoid.	7
2.3	Internal structure of a planar coil.	9
2.4	Coils Shapes	9
2.5	Spiral magn field	10
2.6	Coil spiral	11
2.7	Skin depth	17
2.8	Fskin of Flexar	18
2.9	Skin effect on thicker traces	18
2.10	Proximity effect	19
2.11	Bond graph of the coil-magnet-membrane system.	20
2.12	Coil-Magnet position	21
2.13	Coil-Magnet Transducer bond graph.	22
2.14	Membrane structure	23
2.15	Membrane mat	24
2.16	Bond graph of the membrane-magnet system.	24
2.17	Membrane arms parallel springs.	25
2.18	Final mechanical bond-graph of the membrane and magnet.	25
2.19	Model of two soft fingers grasping the object.	26
2.20	Bond graph of the finger grasping model.	26
3.1	Vibrotactile Sensitivity as a function of the applied pressure force.	29
4.1	Block diagram of the power circuit.	31
4.2	ESP32 16Hz Sine wave generated by the ESP32 Signal Generator software.	32
4.3	Signal conditioning circuit.	33
4.4	Power Op Amp block diagram.	34
4.5	Inverting amplifier circuit.	35
4.6	Inverting amplifier circuit with low-pass filter.	35
4.7	Picture of the implemented power stage.	36

List of Tables

2.1	Physical characteristics of a Flexar coil	14
2.2	Magnetic field remanence of different N grade neodymium magnets. .	21

List of Abbreviations

PCB	Printed Circuit Board
AC	Alternated Current
DC	Direct Current
AI	Artificial Intelligence
CAD	Computer-Aided Design
CNN	Convolutional Neural Network
CPD	Coherent Point Drift
CV	Computer Vision
D	Dimension(s)
DOF	Degrees Of Freedom
EM	Expectation-Maximization
EROSS	European Robotic Orbital Support Services
EU	European Union
FAIR	Facebook's AI Research lab
FOV	Field Of View
GEO	Geostationary Equatorial Orbit
GMM	Gaussian Mixture Model
GPU	Graphics Processing Unit
HRNet	High-Resolution Network
ICP	Iterative Closest Point
IOD	In Orbit Demonstration
LEO	Low Earth Orbit
ML	Machine Learning
MSE	Mean Squared Error
NN	Neural Network
RANSAC	Random Sample Consensus
R-CNN	Region-based Convolutional Neural Network
RPY	Roll, Pitch, Yaw
SIFT	Scale Invariant Feature Transform
SURF	Speeded Up Robust Feature
MSER	Maximally Stable Extremal Regions
BRIEF	Binary Robust Independent Elementary Features
PnP	Perspective-n-Point
SfM	Structure from Motion
SPN	Spacecraft Pose Network
SWaP	Size Weight and Power

List of Symbols

Symbol	Name	Unit
E_{CNN}	Landmark Regression error	px
E_{NN}	Landmark Mapping error	cm
E_T	Translation error	cm
E_R	Rotation error	°
S_T	Translation score	-
S_R	Rotation error	rad

Chapter 1

Introduction

1.1 Thesis objective

In the expanse of space, satellite missions and on-orbit services have become critical assets, serving a myriad of applications including Earth observation, global communication, and scientific research.

The progressive introduction of AI algorithms into various environments, including space applications, represents a significant leap forward in technological advancement. In the context of pose estimation in space, the incorporation of AI brings a multitude of benefits that enhance the autonomy of satellite operations.

In recent years, we've witnessed a rapid proliferation of on-orbit satellites, driven by advancements in technology and the need for enhanced space services. As the number of these satellites continues to rise, the complexities associated with their safe and effective navigation, rendezvous, and scientific missions have grown in tandem. This is where AI shines, as it steps in to revolutionize the field of satellite pose estimation.

AI algorithms, equipped with their machine learning capabilities, enable satellites to process vast amounts of data from onboard sensors with remarkable precision and efficiency. This means an elevated level of accuracy in determining a satellite's position, orientation, and trajectory. But the benefits go beyond mere precision.

AI algorithms, equipped with their machine learning capabilities, enable satellites to process vast amounts of data from onboard sensors with remarkable precision and efficiency. One remarkable development is the ability to estimate a satellite's position and orientation using just a single camera, eliminating the need for a stereo-camera setup. This innovation not only enhances accuracy but also reduces hardware complexity, making satellite design more cost-effective. AI-driven monocular camera-based pose estimation empowers satellites to autonomously process visual data, adjust to dynamic orbital environments, and make informed decisions, even in the midst of complex maneuvers, ensuring the mission's success and safety.

Moreover, the increased autonomy provided by AI minimizes the need for constant human intervention and ground control. This not only reduces operational costs but also allows human operators to focus on more strategic aspects of the mission, enhancing productivity and mission efficiency. As we look to the future, AI algorithms promise to usher in a new era of space exploration and satellite operations.

In summary, the progressive introduction of AI algorithms in space applications, particularly in pose estimation, opens the door to enhanced accuracy, real-time adaptability, autonomy, and overall mission efficiency. This transformative technology propels us closer to unlocking the full potential of space exploration and satellite services.

The objective of this thesis is to implement the rendezvous of a collaborative satellite using AI algorithms, with a particular emphasis on their applications in mono camera-based visual pose estimation. The focus is specifically directed towards a detailed analysis of rendezvous operations within the 200-20cm distance range from a non-cooperative satellite. This project delves into the critical aspects of pose estimation throughout the entire trajectory of the rendezvous process, extending from the initial approach to the final berthing phase.

1.2 Necessary background (?)

1.3 Thesis structure

The thesis is structured in further five chapters:

Chapter 2 - *Background*:

This chapter provides a comprehensive overview of key concepts necessary for the correct understanding of this work, with a focus on monocular camera models, perspective projection, pose estimation, and a general introduction to deep learning models.

Chapter 3 - *State-of-art*:

This chapter delves into monocular pose estimation methods, covering classic approaches like RANSAC and SfM, and exploring modern techniques such as end-to-end learning with networks like PoseNet and Mask R-CNN. The chapter also introduces feature learning, emphasizing CNN-based methods like HRNet for predicting 2D landmark locations. Moreover, some studies about spacecraft pose estimation and their use of deep learning architectures are presented. The chapter also delves into point set alignments, highlighting the widely used and advanced algorithms like Coherent Point Drift (CPD) technique employed in the method for final pose estimation.

Chapter 4 - *Algorithms and Methods*:

This chapter delves into the methodology's core algorithms and techniques. It outlines the offline architecture, detailing the 2D-3D correspondence process, landmark regression, and the neural network-based landmark mapping. The chapter then presents the online architecture, covering real-time processing and the Coherent Point Drift technique for pose estimation. Implementation challenges and dataset considerations are also discussed, providing a comprehensive overview of the applied methods.

Chapter 5 - *Implementation and Experiments*:

This chapter presents the tools and technologies employed for the project implementation and the evaluation metrics for pose estimation, Landmark Regression, Landmark Mapping are described. The chapter culminates in the

assessment of both training and test datasets, showcasing the method's robustness and generalization across diverse scenarios. Overall, it provides comprehensive exploration of the research's implementation and experimentation phases.

Chapter 6 - Discussions and Conclusions:

The Chapter delves into challenges faced by on-board AI systems in space missions, focusing on verifiability and computational load. It emphasizes the significance of minimizing translation errors for accurate maneuvering in the proposed multi-model configuration. The section explores potential improvements, including enhanced landmark selection and strategies to fortify system robustness.

Chapter 2

Background

2.1 Magnetic Coils

2.1.1 Brief History

The connection between electricity and magnetism was first demonstrated by Hans Christian Oersted in 1820 when he observed that an electric current flowing through a wire could deflect a nearby magnetic needle.

Meanwhile, the creation of the first practical electromagnet is credited to William Sturgeon and André-Marie Ampère who after Oersted's discovery experimented with creating coil windings wrapped around an iron core which allowed them to achieve much stronger magnetic fields.

During the 1830's Michael Faraday's discovery of electromagnetic induction further advanced the understanding of magnetic fields and coils. Faraday demonstrated that a changing magnetic field could induce an electric current in a nearby conductor, laying the groundwork for transformers and modern electrical generators.

The latter half of the 19th century saw rapid advancements in electrical engineering. Innovations like early electric generators (dynamoes), transformers, and electric motors heavily relied on magnetic coils for their operation. Researchers such as Nikola Tesla and Thomas Edison further developed these technologies.

Magnetic coils continue to play a vital role in various fields, including power generation, telecommunications, electronics, and medical imaging (such as MRI machines). With advancements in materials science and manufacturing techniques, magnetic coils have become more efficient, compact, and versatile.

In recent years, as the use of PCBs has become widespread, researchers started experimenting with creating coil windings utilizing this technology.

2.1.2 Physics of an inductor?

Inductance

All conductors have some inductance, which may have either desirable or detrimental effects in practical electrical devices. The inductance of a circuit depends on the geometry of the current path and the magnetic permeability of nearby materials.

Any alteration to a circuit that increases the flux (total magnetic field) through the circuit produced by a given current increases the inductance, because inductance is equal to the ratio of magnetic flux to current

$$L = \frac{\Phi(i)}{i} \quad (2.1)$$

Where:

- L is the inductance [H].
- i is the current [A].
- $\Phi(i)$ is the magnetic flux through the circuit [Wb].

Reactance

When a current signal is applied to an inductor, a flux is generated and, considering Faraday's law of induction, any change in flux through a circuit induces an electromotive force \mathcal{E} , proportional to the rate of change of flux

$$\mathcal{E} = -L \frac{d\Phi(t)}{dt} \quad (2.2)$$

Then using Lenz's law, the voltage across the inductor is given by

$$V = -L \frac{di}{dt} \quad (2.3)$$

Inductors resist changes in current due to the magnetic field they generate when current passes through them. When we apply a sinusoidal signal to our inductor, the current will be continuously changing direction. The inductor's opposition to these changes is represented as reactance.

Inductive reactance (X_L) is measured in ohms and is calculated using the formula:

$$X_L = 2\pi fL \quad (2.4)$$

Where:

- X_L = Inductive reactance [Ω]
- f = Frequency of the AC current [Hz]
- L = Inductance of the inductor [H]

We can then calculate the total impedance of the inductor as

$$Z = \sqrt{R^2 + X_L^2} \quad (2.5)$$

Where:

- Z = Total impedance [Ω]
- R = Resistance of the inductor [Ω]
- X_L = Inductive reactance [Ω]

Joule heating

Inductors are passive components, meaning they do not generate energy. However, they do store energy in the form of a magnetic field. When the current through an inductor changes, the magnetic field changes, and energy is stored in the field. When the current decreases, the magnetic field collapses, and the energy is returned to the circuit. This energy is dissipated as heat in the inductor's windings.

The power dissipated in an inductor is given by the relation

$$P = |I_{RMS}|^2 R = \frac{|V_{RMS}|^2}{|Z|^2} R \quad (2.6)$$

Where:

- P = Power dissipated in the inductor [W]
- I = Current flowing through the inductor [A]
- R = Resistance of the inductor [Ω]
- V = Voltage across the inductor [V]
- Z = Total impedance of the inductor [Ω]

Definition of Root Mean Square (RMS) values

As we have seen in the previous paragraphs, the power dissipated by the coil depends on the root mean square values of the current and voltage. We use the RMS values because they allow us to compare the power dissipated by the coil when powered in AC and DC conditions. For DC signals these values are equal to the DC one, while for sinusoidal signals V_{RMS} can be calculated as

$$V_{RMS} = \sqrt{\frac{1}{T} \int_T^0 [f(t)]^2 dt} \quad (2.7)$$

Where:

- T is the period of the input signal
- $f(t)$ is the function of the signal

Then in case we're dealing with AC signals having a DC offset we can use the formula

$$V_{RMS_{AC+DC}} = \sqrt{V_{DC}^2 + V_{RMS_{AC}}^2} \quad (2.8)$$

Some formulas for important waveforms:

2.1.3 Magnetic field generation

The strength of the magnetic field on the z-axis of the coil is derived from the Biot-Savart Law and is given by the formula

$$B_z = \frac{N\mu I r^2}{2(r^2 + z^2)^{\frac{3}{2}}} \quad (2.9)$$

Name	Waveform	V_{RMS}
DC	V_P	V_P
Sine Wave $[-V_P, V_P]$	$V_P \sin(2\pi ft)$	$\frac{V_P}{\sqrt{2}}$
Polarized Sine Wave $[0, V_P]$	$\frac{V_P}{2} (\sin(2\pi ft) + 1)$	$\frac{V_P}{2} \sqrt{\frac{3}{2}}$
Square Wave $[-V_P, V_P]$	$V_P \text{sgn}(\sin(2\pi ft))$	V_P
DC-shifted Square Wave $V_{DC} + [-V_P, V_P]$	$V_{DC} + V_P \text{sgn}(\sin(2\pi ft))$	$\sqrt{V_{DC}^2 + V_P^2}$

FIGURE 2.1: RMS values for different waveforms.

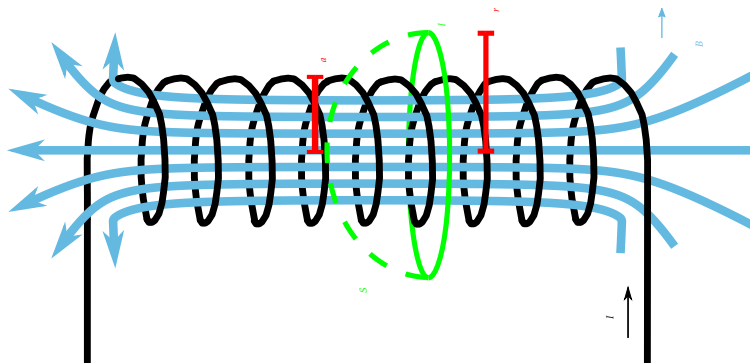


FIGURE 2.2: Magnetic field generated by a solenoid.

Where:

- B_z is the magnetic field on the z-axis [T].
- μ is the magnetic permeability of the medium [H/m].
- I is the current flowing through the wire [A].
- r is the radius of the coil [m].
- N is the number of turns of wire in the coil.
- z is the z-distance from the center of the coil [m].

If the coil lacks a core the permeability of free space is used instead of the core's permeability; instead if wound on a ferromagnetic core the permeability of the core is calculated as

$$\mu = \mu_0 \cdot \mu_r$$

where μ_r is the relative permeability of the core material.

With the right material for the core, the magnetic field intensity can be highly increased compared to the field generated by the coil alone.

Magnetic Flux and Field relation

We can also relate the magnetic field to the magnetic flux generated by the coil. The magnetic flux is given by the formula

$$\Phi_B = B \cdot A \quad (2.10)$$

Where:

- Φ_B is the magnetic flux [Wb].
- B is the magnetic field [T].
- A is the area of the coil [m²].

2.2 PCB Coils

The biggest problem with standard coils is their size, especially in the z-direction as the more windings are used the thicker they will become. This is a problem for applications where space is limited, such as in the case of implantable devices. To address this issue, researchers have started to experiment with creating coil windings using PCB technology. This allows for the creation of coils that are thinner and more compact than traditional coils. In this section, we will discuss the different types of PCB coils and the challenges associated with their miniaturization.

2.2.1 Planar coils

As PCBs are 2D objects we can't work on the z-axis to create the coil's windings. This means that the windings have to be created on the same plane. In 1984 researchers from Osaka University proposed the first implementation of a possible solution in the form of planar coils. They proposed and tested a structure comprised of concentric spirals, with different shapes, made of a conductive material (mostly copper)

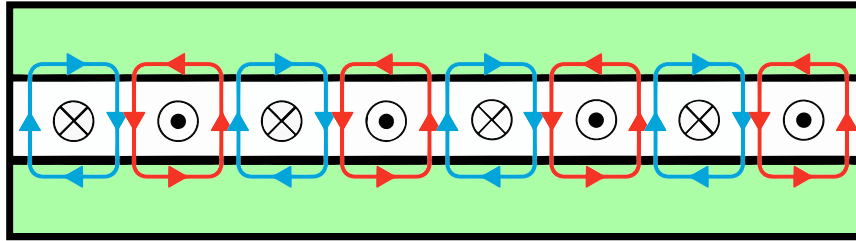


FIGURE 2.3: Internal structure of a planar coil.

suspended in an insulation material and then covered by two magnetic material layers (???) [5].

With the mainstream adoption of PCBs in the electronics industry, researchers have created planar coils using PCBs by etching spiral patterns on the copper layer. This allowed for the production of planar coils easily and cheaply.

The main advantage of planar coils is that they can be easily integrated into the PCB design, reducing the overall size of the device. This is particularly useful in the case of wireless power transfer systems, where the coils are used to transfer power between devices. The smaller size of the coils allows for more compact and portable devices.

Another advantage is the ability to design coils of arbitrary shapes and sizes, depending on the requirements of the application. This flexibility allows for the creation of coils that are optimized for specific applications and PCB shapes, resulting in improved performance.

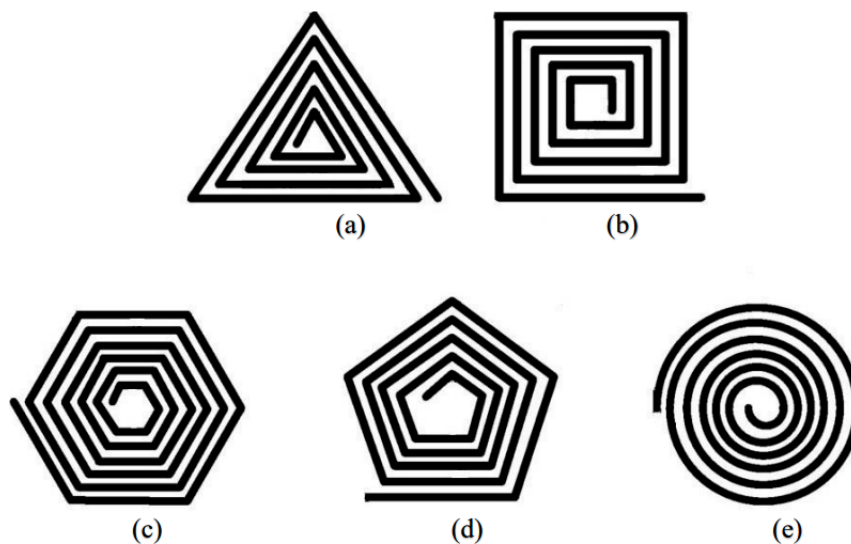


FIGURE 2.4: Different planar coil architectures such as (a) triangle, (b) square, (c) pentagon, (d) hexagon, (e) circle.

2.2.2 Planar coil magnetic field

The structure of a planar coil is very different from a standard one, as it is a flat structure with a spiral winding. The magnetic field generated by a planar coil is more complex than that of a standard coil, as the magnetic field is not concentrated

in the center of the coil but is distributed over the entire surface of the coil. The magnetic field generated by a planar coil is represented in Figure 2.5

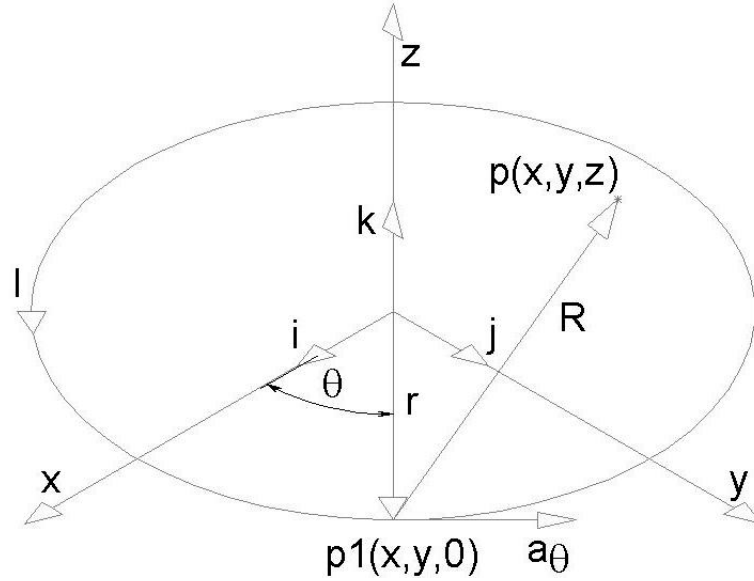


FIGURE 2.5: (c) Representation of the magnetic field generated by a circular spiral planar coil placed on an aluminum plate.[3]

Then considering again the circular spiral structure, the magnetic field generated by a planar coil at its surface can be derived as

$$B_z = \frac{\mu N I}{2} \cdot \frac{\ln(\frac{b}{a})}{b - a} \quad (2.11)$$

Where:

- B_z is the magnetic field on the z-axis [T]
- μ is the magnetic permeability of the medium [H/m]
- n is the number of turns of the spiral
- I is the current flowing through the wire [A]
- b is the external radius of the spiral [m]
- a is the internal radius of the spiral [m]

To then find the magnetic field at a distance z from the center of the coil, we can use the equation 2.9 from the previous subsection and substitute the radius r of the coil with

$$r' = \frac{b - a}{\ln \frac{b}{a}} \rightarrow B_z = \frac{\mu N I r'^2}{2(r'^2 + z^2)^{\frac{3}{2}}} \quad (2.12)$$

2.2.3 Multi-layer PCB coils

Another approach to miniaturizing PCB coils is to create multi-layer coils. This is done by stacking multiple layers of PCBs on top of each other, with each layer containing a different part of the coil. This allows for the creation of coils with a higher

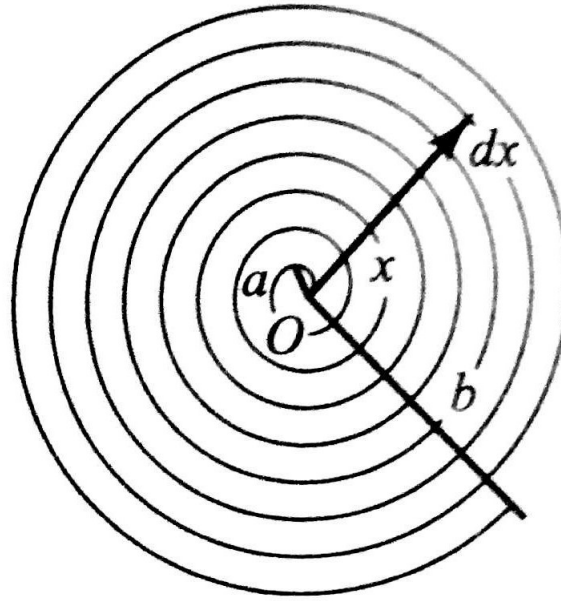


Fig. S2.75

FIGURE 2.6: Circular spiral coil.

number of windings in a smaller space. The main challenge with multi-layer PCB coils is the alignment of the different layers. If the layers are not aligned properly, the coil will not function correctly.

Current manufacturing allows for up to 10 layers of PCBs to be stacked on top of each other. However, the more layers that are added, the more difficult it becomes to align the layers correctly. If the layers are not aligned properly, the magnetic field generated by each layer will also not be aligned, which can lead to a decrease in the efficiency of the coil due to interferences.

Total inductance

Considering a two layers coil the total inductance can be calculated as

$$L_s = 2L_0 + 2M, M = K_c \cdot L_0 \quad (2.13)$$

Where:

- L_s is the total inductance of the coil [H].
- L_0 is the inductance of a single layer [H].
- M is the mutual inductance between the two layers [H].
- K_c is the coupling coefficient between the two layers.

Then K_c can be calculated with an empirical formula derived from multiple measurements by Jonsenser Zhao [17] as

$$K_c = \frac{N^2}{0.64[(0.184d^3 - 0.525d^2 + 1.038d + 1.001)(1.67N^2 - 5.84N + 65)]} \quad (2.14)$$

Where:

- N is the number of turns of the coil.
- d is the distance between the two layers [m].

Magnetic field generated by a Multilayer coil

We can use equation 2.1 and L_s calculated in the previous point to find the magnetic flux through the coils

$$\Phi(I) = L_s \cdot I \quad (2.15)$$

Then with equation 2.10 we can derive the total magnetic field as

$$B_t = \frac{L_s \cdot I}{\pi r^2} \quad (2.16)$$

Where:

- B_t is the total magnetic field [T].
- r is the radius of the coil [m].

2.3 Flexible PCB coils

Flexible PCB coils are a type of PCB coil that is made using a flexible substrate. This allows for the creation of coils that can be bent and twisted without breaking.

2.3.1 Pros of flexible coils

Flexible PCBs (Printed Circuit Boards) offer several advantages over traditional rigid PCBs. Here are some of the key pros of flexible PCBs:

1. **Flexibility and Space Savings:** Flexible PCBs can bend and twist, allowing for compact and efficient use of space in electronic devices.
2. **Lightweight:** The materials used in flexible PCBs are lightweight, making them ideal for applications where weight is a concern, such as in aerospace or portable electronics.
3. **Improved Design Freedom:** Flex PCBs allow for more creative and versatile designs because they can be formed into complex shapes and fit into tight or irregular spaces.
4. **Reduced Connectors and Interconnects:** Because flexible PCBs can bend, they can often eliminate the need for additional connectors and interconnects, reducing overall system complexity.
5. **Vibration and Shock Resistance:** Flexible PCBs can absorb shock and vibrations better than rigid PCBs, making them suitable for use in environments where these are concerns.

6. **Simplified Assembly:** With fewer connectors and interconnects, assembly becomes easier and faster, reducing labor and potential points of failure.
7. **High-Density Interconnects:** Flexible PCBs can support fine-pitch components and high-density interconnects, making them suitable for advanced electronics.

2.3.2 Application challenges

As said before flexible PCBs offer great design flexibility and the possibility of implementing innovative designs and devices but they also come with their own set of challenges; especially in the case of flexible coils.

Rise of high resistance

Taking as an example the flexible coil we'll be using in our project, the resistance of the coil is 30Ω . This is a relatively high resistance for a coil, especially when compared to traditional copper wire coils. This is due to the intrinsic structure of PCBs, especially flexible ones. PCBs are created by etching very thin copper traces on a substrate, in the case of flexible PCBs, as the substrate must be flexible, their thickness is even lower and consequently also the traces are.

The coil can be considered as a very long strand of a very thin copper so its resistance can be calculated using the Ohm Law

$$R = \rho \cdot \frac{L}{A} \quad (2.17)$$

Where:

- R is the resistance [Ω].
- ρ is the resistivity of the material [$\Omega \cdot m$].
- L is the length of the conductor [m].
- A is the cross-sectional area of the conductor [m^2].

Then to find the length of the copper traces we can use the approximated formula [15]

$$L = N\pi \frac{D + d}{2} \quad (2.18)$$

Where:

- N is the number of turns.
- D is the outer diameter of the coil [m].
- d is the inner diameter of the coil [m].

The tracks' cross-section is a rectangle so the area can be calculated as

$$A = w \cdot t \quad (2.19)$$

Where:

- w is the width of the track [m].

- t is the thickness of the copper [m].

Finally considering the physical characteristics of our coil

Coil Specifications	
Track (width/spacing)	$4/4mil = 1.016e - 4/1.016e - 4m$
Turns	$2*35$ (two coils in series)
Radius	$7.9e - 3m$
Copper thickness	$0.5oz = 1.74e - 5m$
Resistivity	$1.72e - 8\Omega m$
Maximum Constant Power	$0.8W$

TABLE 2.1: Physical characteristics of a Flexar coil

The Length of the tracks (considering both spires) will be $L = 3.4548m$ and the cross-section area will be $A = 1.7678e - 09m^2$. As we can observe we have a wire which is both very long and very thin so a high resistance is expected (from the calculation $R = 33.61\Omega$).

Also, the resistance of the coil is dependent on the Temperature of the coil, as the temperature increases the resistance of the copper increases as well. This is because the resistivity of copper increases with temperature. This is a problem as the coil releases a lot of heat when powered with high currents.

The temperature coefficient of resistivity of copper is $\alpha = 0.003862 \frac{1}{^\circ C}$ so the resistivity of copper at a certain temperature can be calculated as

$$\rho(T) = \rho_{T_{ref}} \cdot (1 + \alpha \cdot (T - T_{ref})) \quad (2.20)$$

Where:

- $\rho_{T_{ref}}$ is the resistivity at the reference temperature [$\Omega \cdot m$].
- α is the temperature coefficient of resistivity [$\frac{1}{^\circ C}$].
- T is the temperature [$^\circ C$].
- T_{ref} is the reference temperature [$20^\circ C$].

Joule effect

As said before, a coil of this type releases a lot of heat when powered with high currents. This is also due to its high resistance. The heat dissipation of a coil can be calculated using the formula

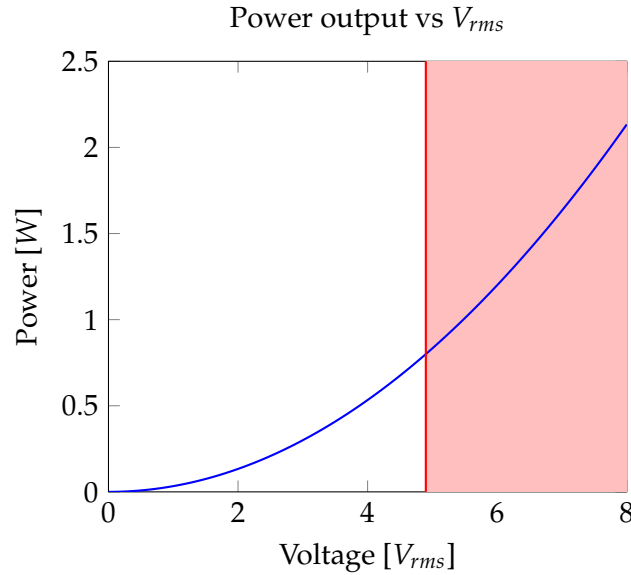
$$P = I_{RMS}^2 R = \frac{V_{RMS}^2}{R} \quad (2.21)$$

Where:

- P is the power dissipated by the coil [W].
- I_{RMS} is the root mean square current [A].
- V_{RMS} is the root mean square voltage [V].

- R is the resistance of the coil [Ω].

The coil can dissipate a maximum of 0.8W of power, this is a very low value and it is very easy to surpass it. This is a problem as the coil can be damaged if it dissipates more power than it can handle.



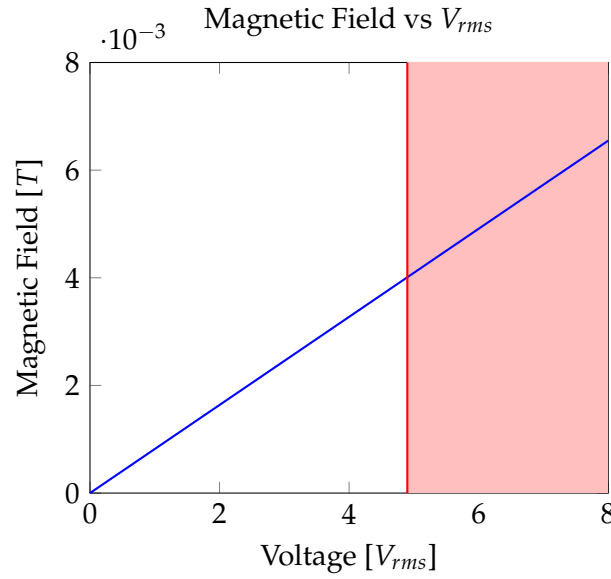
When exceeding the limit, even if the coil doesn't get damaged, the heat it releases can affect the performance of the coil. The coil's resistance increases with temperature, so the coil will dissipate even more power, this can lead to a thermal runaway situation where the coil will keep increasing its temperature until it gets damaged.

The only solution could be to introduce a heat sink to dissipate the heat but for the amount needed to be managed, we will show that flexible solutions aren't enough.

Magnetic field strength

As the coil can't be run at high currents, the magnetic field it generates will be very weak, this will affect the performance of the coil as the magnetic field is what allows the coil to interact with the environment. This is a problem as the coil will be less sensitive and will have a shorter range.

Considering the Flexar coil as an example we can plot the magnetic field strength, at the surface, as a function of the voltage applied to the coil using equation 2.11 (considering the coil as a parallel of two spirals)



As we can observe even at the power limit of 0.8W ($\simeq 5V$) the magnetic field generated by the coil is very low ($\simeq 4mT$).

Resistance parasitic effects due to AC current

This paragraph will be a brief introduction to the parasitic effects that can occur in a coil due to the AC current that flows through it. All these effects are negligible at low frequencies (up to about 1kHz) which is the range we are aiming for in this project, but we will explore them for the sake of future research.

The main parasitic effects that can occur in a coil are:

- **Reactance:** This is the opposition that a coil offers to the flow of AC current. This is due to the self-inductance of the coil which opposes the change in current flowing through it. This effect can lead to a change in the effective resistance of the coil.

The reactance of a coil can be calculated using the formula

$$X_L = 2\pi fL \quad (2.22)$$

Where:

- X_L is the reactance of the coil $[\Omega]$.
- f is the frequency of the AC current $[Hz]$.
- L is the inductance of the coil $[H]$.

Then the impedance of the coil can be calculated as

$$Z = \sqrt{R_{DC}^2 + X_L^2} \quad (2.23)$$

- **Skin effect:** This effect is due to the current flowing through a conductor tending to flow on the surface of the conductor. This gives rise to a thin layer inside the conductor where all the current flows. As a result, the effective resistance of the conductor increases. This effect is more pronounced at higher frequencies.

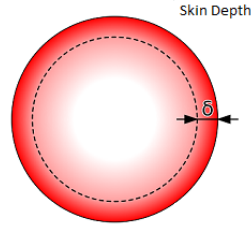


FIGURE 2.7: (c) Representation of the thin surface generated by the skin effect

The thickness of this area is called the **skin depth** and can be calculated using the formula

$$\delta = \sqrt{\frac{\rho}{\mu\pi f}} \quad (2.24)$$

Where:

- δ is the skin depth [m].
- ρ is the resistivity of the conductor [$\Omega \cdot m$].
- μ is the magnetic permeability of the medium [H/m].

The effective resistance of the conductor can be derived from the skin depth using Dowell's equation

$$R_{skin} = F_{skin} \cdot R_{DC} \quad (2.25)$$

and

$$F_{skin} = \frac{1}{2} \left(\frac{h}{\delta} \right) \frac{\sinh(\frac{h}{\delta}) + \sin(\frac{h}{\delta})}{\cosh(\frac{h}{\delta}) - \cos(\frac{h}{\delta})} \quad (2.26)$$

Where:

- R_{skin} is the effective resistance of the conductor due to the skin effect [Ω].
- F_{skin} is the skin effect factor.
- h is the thickness of the conductor [m].

In the case of the coil we're studying, the skin effect is negligible up to $1e8Hz$ as the thickness of the flexible PCB's traces is very low.

But we can observe from the study done on thicker traces' (0.5mm) coils that the skin effect starts to be already noticeable at $1e5Hz$.

- **Proximity effect:** This effect is similar to the skin effect but it occurs when two conductors are close to each other. The current flowing through one conductor induces an eddy current in the other conductor which can lead to a change in the effective resistance of the conductors.

The contribution of the proximity effect to the effective resistance of the coil can be calculated using the formula (considering current flowing in the coil $I_{ex} = 1A$) [9]

$$R_{proximity} = \frac{1}{12} h \sigma \pi^2 f^2 B_n^2 w^3 \quad (2.27)$$

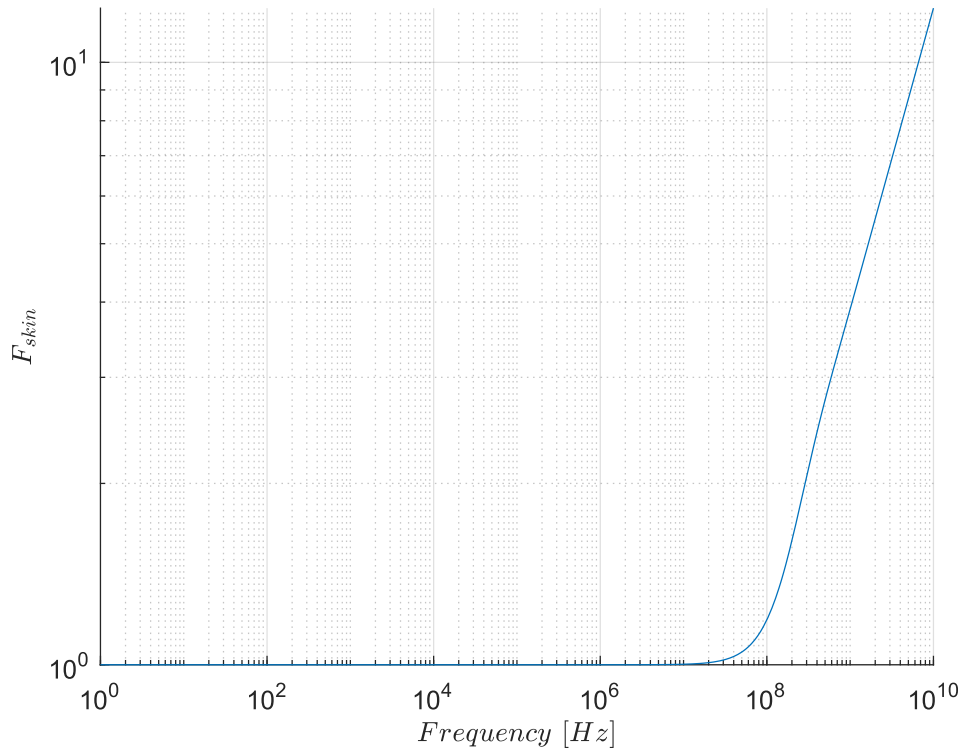


FIGURE 2.8: Logarithmic plot of the skin effect factor for a flexible PCB coil

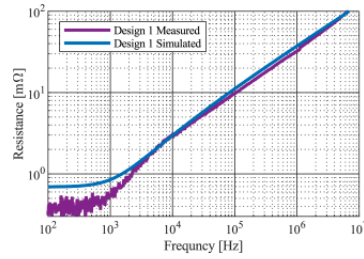


FIGURE 2.9: Skin effect on thicker traces [10]

Where:

- σ is the conductivity of the conductor [$\Omega^{-1} \cdot m^{-1}$].
- h is the thickness of the conductor [m].
- f is the frequency of the AC current [Hz].
- B_n is the average external magnetic field [T].
- w is the width of the conductor [m].

We can also approximate $F_{proximity}$ ($F_{proximity} = R_{proximity} / R_{DC}$) as

$$F_{proximity} = \frac{F_{skin}}{3} \quad (2.28)$$

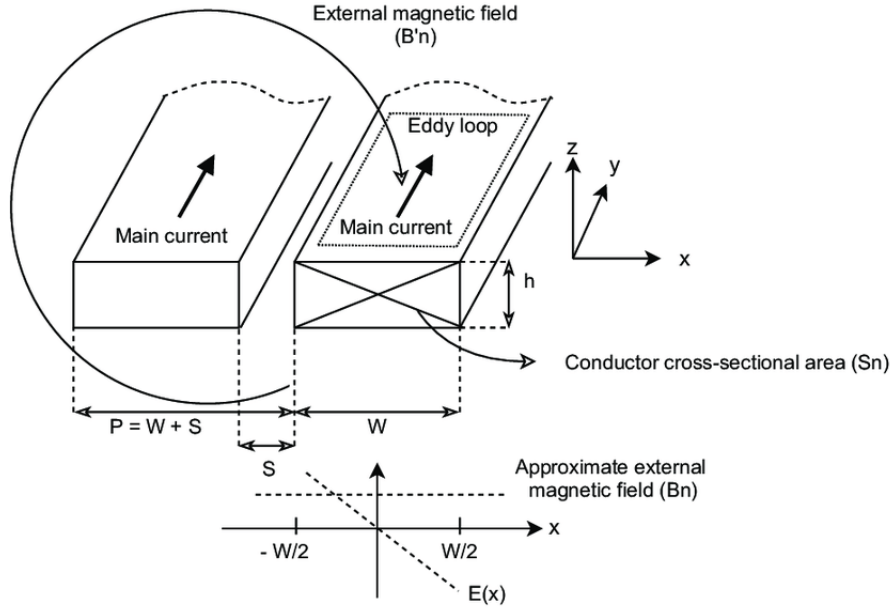


FIGURE 2.10: Representation of the proximity effect

So when the contribution of the skin effect is negligible, the proximity effect will be negligible as well.

2.3.3 Running flexible PCB coils

High current needs

As discussed in the previous paragraph flexible coils have very high resistance so to produce even low magnetic fields high current must be provided. Considering the power limit of the Flexar coil $P_{max} = 0.8W$ we can calculate the maximum current that can be provided to the coil with 2.6 as

$$I = \sqrt{\frac{P_{max}}{R}} = \sqrt{\frac{0.8}{30}} = 0.1633A \quad (2.29)$$

Constant Voltage vs Constant Current power supplying

To power our coil we have two options, we can either provide a constant voltage or a constant current. Using a constant current source is not advisable due to the heating problem of the coil, at high currents as the coil is run it will heat up and its resistance will increase which will cause the power source to increase the voltage to keep the current constant. This in turn will cause the coil to heat up even more and the cycle will continue until the coil is damaged.

Instead, using a constant voltage source as the resistance increases due to the coil exceeding the heating and power threshold we will only have a decrease in the current which results in a loss of magnetic field strength but the coil won't get damaged.

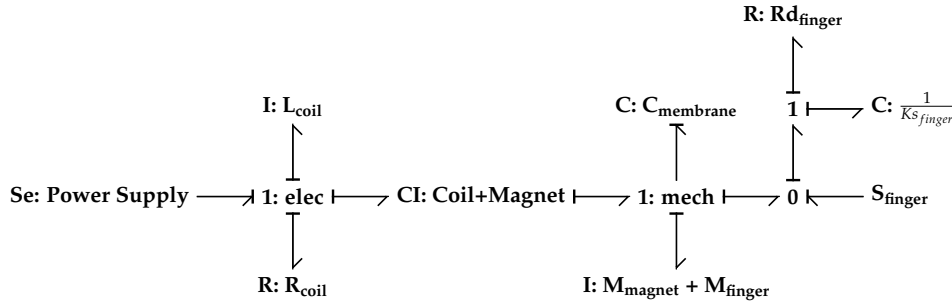


FIGURE 2.11: Bond graph of the coil-magnet-membrane system.

2.4 Modelling of the Entire System

To be able to produce vibrations using the magnetic field produced by the coil we need to introduce to the system an object that can react to the magnetic field. As the magnetic field of the coil is very feeble we can use as the object Neodymium magnets, these are permanent magnets with a very strong internal magnetic field for their size. Using small ones and with the right pole facing the coil (same polarity as the generated magnetic field) it will be able to repel them and make them vibrate. Then to constrain the motion of the magnet and make it only move in the z -axis we have to add to the system a flexible membrane.

We can now model the entire system using a bond graph, as shown in figure 2.11.

In the next subsections, we will analyze the physical laws that govern the behavior of the system and how to model them to create this bond graph.

2.4.1 Neodymium magnets (magnetic strength wrt class and dimensions)

Neodymium magnets are a type of rare-earth magnet, they are the strongest type of permanent magnets made commercially. They are made of an alloy of neodymium, iron, and boron and their strength depends on the percentage of neodymium in the alloy and on its crystalline structure. They are classified based on their maximum energy product, which is the maximum amount of energy that can be stored in a magnet. Modern neodymium magnets start from N35 and go up to N52 (even N55), the higher the number the stronger their magnetic field.

Considering a cylindrical magnet with a radius R_M and a thickness t we can calculate the magnetic field generated by it at a distance z from a pole surface using the formula [14]:

$$B_M(z) = \frac{B_r}{2} \left(\frac{t+z}{\sqrt{R_M^2 + (z+t)^2}} - \frac{z}{\sqrt{R_M^2 + z^2}} \right) \quad (2.30)$$

Where:

- B_r is the remanence of the magnet [T]
- R_M is the radius of the magnet [m]
- t is the thickness of the magnet [m]
- z is the distance from a pole surface of the magnet [m]

Goudsmit Grade	Remanence B_r [mT]	
	min value	typical value
N35	1170	1210
N38	1220	1260
N40	1260	1290
N42	1290	1320
N45	1320	1370
N48	1370	1420
N50	1400	1460
N52	1420	1470

TABLE 2.2: Magnetic field remanence of different N grade neodymium magnets.

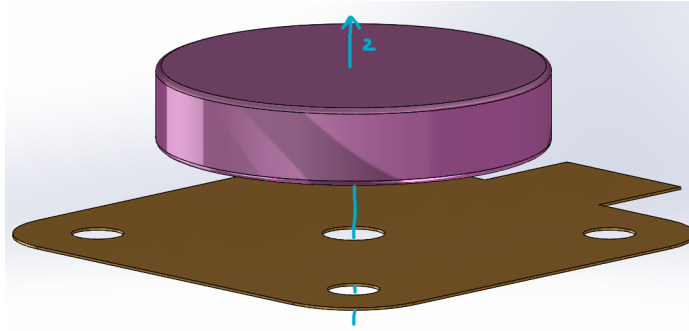


FIGURE 2.12: Coil and magnet position in space.

The remanence of a magnet is the magnetic field that remains in the magnet after the external magnetic field is removed and depends on the N grade of the magnet.

2.4.2 Magnetic force between magnet and coil

To calculate the magnetic repulsion force between the coil and a permanent magnet we consider them aligned with their centers coinciding on the z-axis.

The force between a magnet and a coil can be calculated using the magnetic field generated by the coil and magnet. Knowing their closed-form expression we can calculate the force using this formula:

$$F = \nabla(\vec{m}_M \cdot \vec{B}_C) \quad (2.31)$$

Where:

- \vec{m}_M is the magnetic moment of the magnet [A/m]
- \vec{B}_C is the magnetic field generated by the coil [T]

The magnetic momentum of the magnet is defined as:

$$\vec{m}_M = \begin{pmatrix} 0 & 0 & \frac{B_M(z)}{\mu} \end{pmatrix} \quad (2.32)$$

Where:

- $B_M(z)$ is the magnetic field generated by the permanent magnet [T]



FIGURE 2.13: Coil-Magnet Transducer bond graph.

$$F(q, i) = \frac{1}{2} \frac{d(L(q) \cdot m_M(q))}{dq} i \quad (2.35)$$

$$\lambda = L(q)i \quad (2.36)$$

- μ is the magnetic permeability of the medium [H/m]

We can calculate the magnetic field generated by the coil at a distance using equation 2.12 (considering our coil as two in parallel) and the magnetic field generated by a cylindrical magnet at a distance z using equation 2.30.

Doing the calculations, the resulting force in function of the distance z is given by:

$$F = \frac{B_r I N R_C^2 \left(\frac{1}{\sqrt{\sigma_1}} - \frac{1}{\sqrt{\sigma_2}} + \frac{z^2}{\sigma_2^{3/2}} - \frac{2(t+z)^2}{2\sigma_1^{3/2}} \right)}{2\sigma_3^{3/2}} + B_C(I) \cdot \frac{3z \left(\frac{z}{\sqrt{\sigma_2}} - \frac{t+z}{\sqrt{\sigma_1}} \right)}{2\sigma_3} \quad (2.33)$$

Where:

- N is the number of spires of a one-layer coil
- I is the current flowing through the coil [A]
- B_C is the coil magnetic field calculated as in 2.12 [T]
- R_C is the coil average radius (r' in equation 2.12) [m]
- $\sigma_1 = R_M^2 + (t+z)^2$
- $\sigma_2 = R_M^2 + z^2$
- $\sigma_3 = R_C^2 + z^2$

So we can model the coil-magnet system as a **Transducer** element that converts the current flowing through the coil into a force acting on the magnet.

$$B_C(z, I) = \frac{\mu N I R_C^2}{2(R_C^2 + z^2)^{3/2}} \rightarrow B_C(q, i) = \frac{1}{2} L(q) i \quad (2.34)$$

2.4.3 Membrane-magnet system

The magnet needs to be suspended to allow it to move freely only on the z -axis, to achieve this we need a structure that constrains the lateral motion of the magnet and needs to also be able to vibrate freely with it. To do this we can use a flexible membrane that can deform under the magnetic field generated by the coil and the magnet.

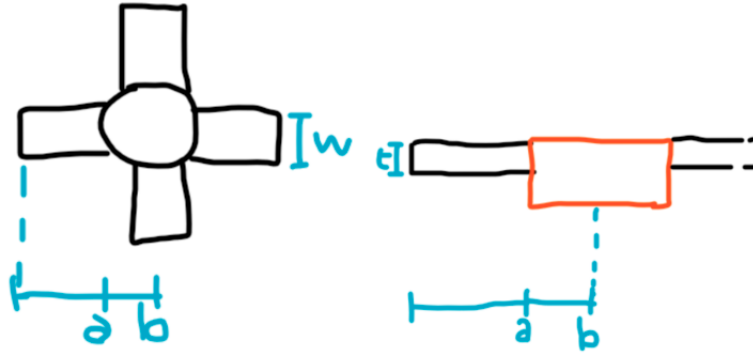


FIGURE 2.14: Membrane structure of the last prototype.

As an example, we will analyze the membrane structure of the last type of prototype we implemented

This membrane is a simple Celtic-cross structure made of thin silicone integrated with the entire structure of the device, the membrane is built with a central cylindrical chamber used to trap the magnet in the center of the cross.

The membrane can be modeled as a mass-spring-damper system.

Membrane stiffness

The membrane stiffness can be calculated using Young's modulus of the material and the geometry of the membrane. Each arm of the cross can be considered as a cantilever beam, the stiffness of a cantilever beam can be calculated as:

$$k_s = \frac{3EI_x}{L^3} \quad (2.37)$$

Where:

- k_s is the stiffness of the membrane's arm [N/m]
- E is the Young's modulus of the material [Pa]
- I is the second moment of inertia of the arm [m⁴]
- L is the length of the arm [m]

The arm can be simplified as a parallelepiped with a rectangular section, and the second moment of inertia on x can be calculated as:

$$I_x = \frac{wt^3}{12} \quad (2.38)$$

Where:

- I_x is the second moment of inertia on the x-axis [m⁴]
- w is the width of one membrane arm as in figure 2.14[m]
- t is the thickness of the membrane as in figure 2.14[m]

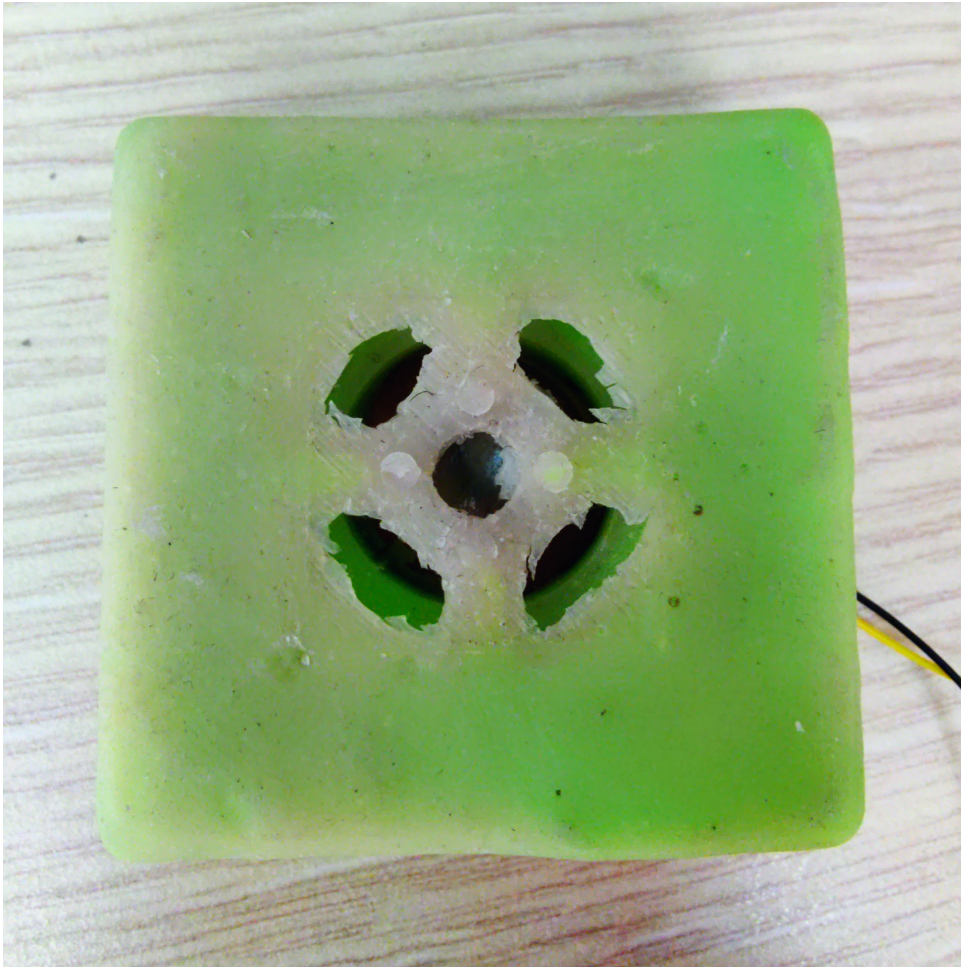


FIGURE 2.15: Membrane of the last prototype with the magnet trapped in the center.

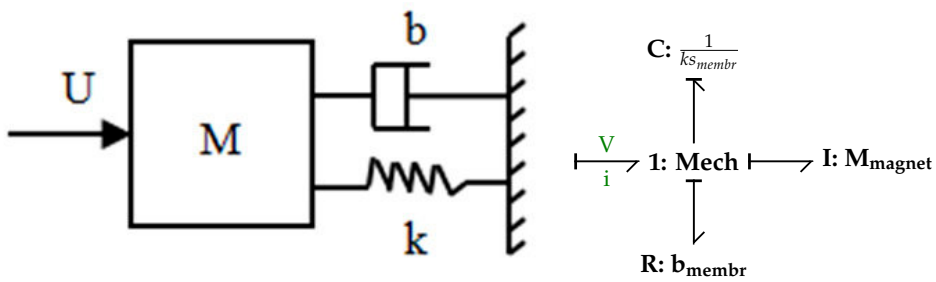


FIGURE 2.16: Bond graph of the membrane-magnet system.

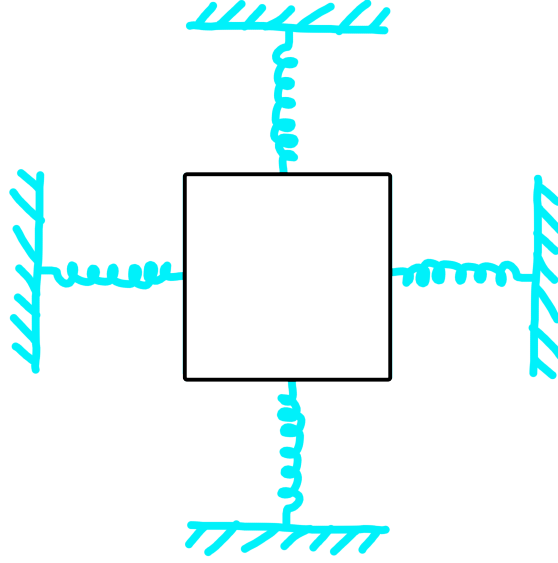


FIGURE 2.17: Membrane arms parallel springs.

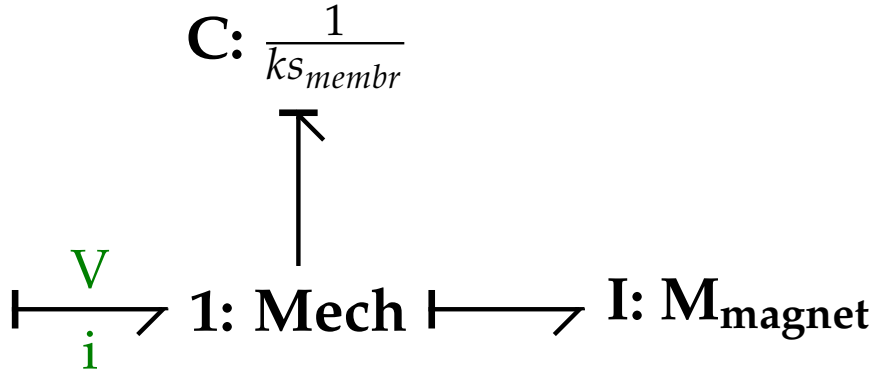


FIGURE 2.18: Final mechanical bond-graph of the membrane and magnet.

Then we can consider the 4 arms as 4 springs in parallel, the total stiffness of the membrane can be calculated as:

$$ks_{membr} = 4ks \quad (2.39)$$

Membrane damping

The damping for a cantilever beam is neglectable, so we can remove the resistive component from the mechanical model.

2.4.4 Finger grasping model

At last, we have also to model the finger grasping the device, we can derive the model from the one used in [6] for the human finger.

This model describes two fingers grasping an object, for our case, we can simplify it to a single finger grasping the device. Also, we can neglect the friction between the finger and the device as the device will be tested positioned on a flat surface with only the finger touching it from above.

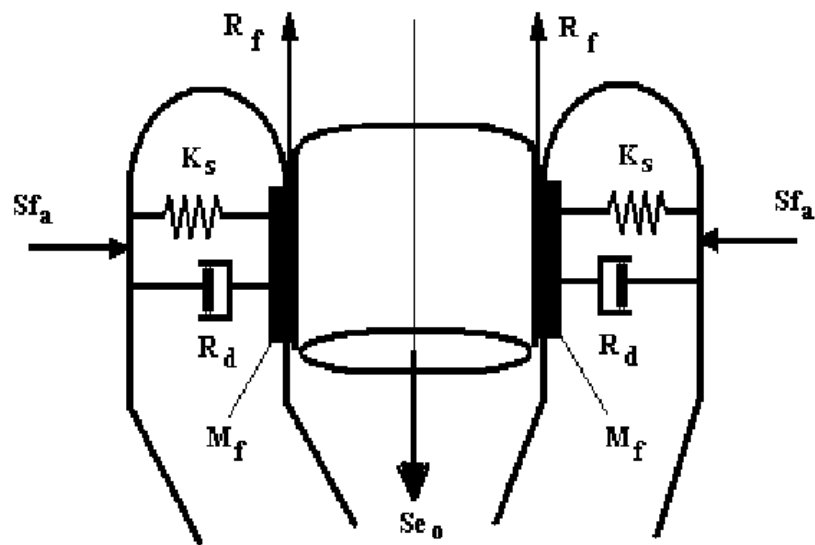


FIGURE 2.19: Model of two soft fingers grasping the object.

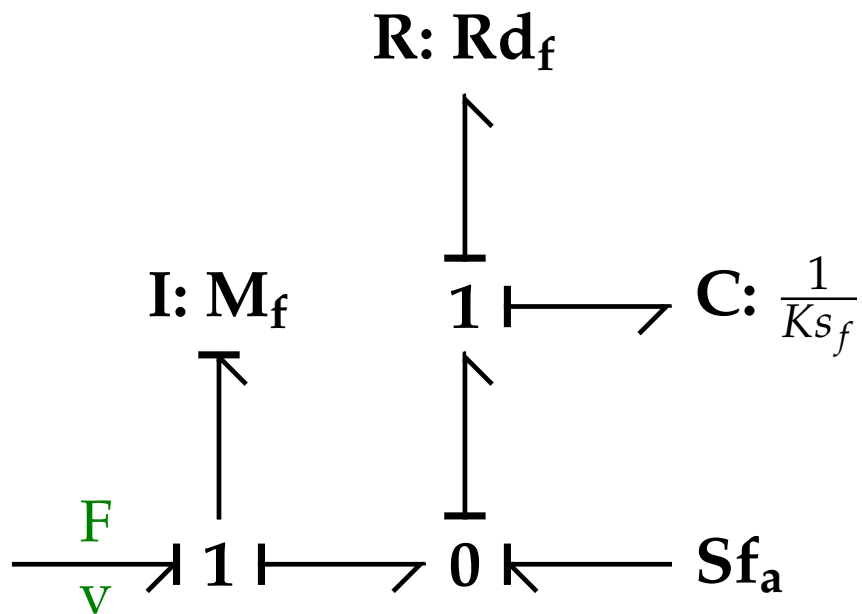


FIGURE 2.20: Bond graph of the finger grasping model.

Chapter 3

Overview of Haptic Feedback

Computer Haptic Feedback or Haptics, in short, is the research field that deals with the need to be able to digitalize the human sense of touch and reproduce it. Despite the research done in this field since the mid-20th century, the technology is still in its infancy. The main reason for this is the complexity of the human sense of touch which we still don't understand fully. This, in turn, doesn't allow us to even approximately match the capabilities of the human sense of touch; but we can still use this infant technology to reproduce simple sensations. This sensation can be used in many fields, from the entertainment industry to the medical field, from the military to the automotive industry to convey information that we do not normally acquire via touch, such as notifications and warnings related to particular events, guidance instructions, and even crude reproduction of textures. In this chapter, we will give an overview of the human sense of touch and the state of art technologies used to reproduce it.

3.1 Physics of Haptic Feedback

3.1.1 Biology of Haptic Sensing

The human tactile sensing system can measure specific properties of materials, such as temperature, texture, shape, force, fine-form features, mass distribution, friction, hardness and viscoelasticity, through physical contact between the human skin and the object. Even the changing state of the interaction, such as gravitational and inertial effects, can be perceived through the sense of touch. As the sensing system works through the skin, it doesn't rely on a localized sensory organ but behaves as a distributed system, also different parts of the body have different thresholds of sensitivity. For these reasons, it's difficult to treat a tactile signal as a well-defined quantity like visual and audio signals and its complex nature makes it difficult to replicate its functioning in science or engineering tasks.

The sense of touch is based on the somatosensory system, which is a complex system of nerve endings and touch receptors in the skin. The somatosensory system is composed of four main types of receptors:

- **Mechanoreceptors** - These are the most common type of tactile receptors in the skin. They are responsible for sensing pressure, vibration, stretching, and brushing.
- **Thermoreceptors** - These receptors are responsible for sensing temperature changes in the skin. There are two main types of thermoreceptors: warm receptors and cold receptors.

- **Nociceptors** - These receptors are responsible for sensing pain and tissue damage. They are activated by noxious stimuli, such as extreme temperatures, pressure, or chemicals.
- **Proprioceptors** - These receptors are responsible for sensing the position and movement of the body. They are located in the muscles, tendons, and joints, and provide feedback to the brain about the relative position between different parts of the body.

The most important receptors for haptic feedback are the mechanoreceptors, they react to mechanical stimuli by producing signals in the form of streams of voltage pulses at high frequencies, the stronger the stimuli higher the frequency of the pulses. When the cell adapts to the stimulus, the pulse frequency subsides to its normal rate. Considering the goal of this research we can focus on the mechanoreceptors that are responsible for sensing pressure and vibration, these are the Pacinian corpuscles and the Meissner corpuscles. The first ones are more sensible to high-frequency vibrations (200-550Hz), while the second ones are more for low-frequency vibrations (20-40Hz). [2]

3.1.2 Haptic sensitivity

As the mechanoreceptors are enveloped in various skin layers, their sensitivity to vibrations will not be infinite. The strength of the sensation will depend on the frequency and amplitude of the vibration. The amplitude of the vibration can be considered in terms of the acceleration of the membrane-magnet system. Previous works [11] found that, for a pulp contact area ranging from 53 to 176.7 mm², the threshold of detection of vibrations was between 0.1778 and 0.5623 m/s² (in the work specified as 105-115 dB (re 1e-6m/s²)) for sinusoidal stimuli ranging from 100 to 250 Hz.

+ For frequencies close to 125Hz the threshold should also lower as the finger pulp reaches its resonance frequency [16].

The study also highlights that the sensitivity depends on the constant pressure force applied on the skin in conjunction with the vibration. They found that under active pressing force, the sensitivity threshold decreases to 0.027-0.143 m/s² (in the work specified as 68.5-83.1 dB (re 1e-6m/s²)) for a constant applied force of 1.6N.

For higher pressure forces the sensitivity threshold decreases even further Fig. 3.1.

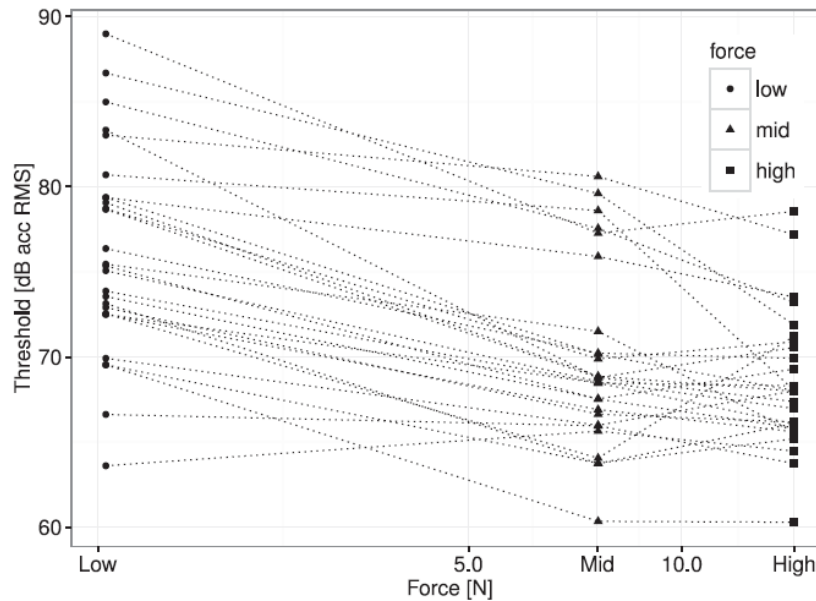


FIGURE 3.1: Vibrotactile Sensitivity as a function of the applied pressure force.

3.2 State of the Art in vibrotactile haptic feedback

For now, state of the art in haptic feedback is still in its infancy. The main reason for this is the complexity of the human sense of touch which we still don't understand fully. The best technology we have for now to reproduce haptic feedback through vibrotactile means is the piezoelectric actuator.

3.2.1 Piezoelectric actuators

Piezoelectric actuators are a very interesting technology based on the piezoelectric effect. Materials exhibiting this effect, such as certain ceramics and crystals, possess the ability to convert electrical energy into mechanical motion, and vice versa.

The operating principle of piezoelectric actuators relies on the application of an electric field across the piezoelectric material. This electric field induces a deformation within the material, causing it to expand or contract depending on the polarity of the applied voltage. This minute deformation translates into highly precise mechanical displacement, enabling piezoelectric actuators to achieve nanometer-scale resolutions with remarkable speed and accuracy.

One of the defining characteristics of piezoelectric actuators is their rapid response time. Unlike traditional electromagnetic actuators, which may suffer from inertia and mechanical backlash, piezoelectric actuators can swiftly change their state in response to electrical signals.

Frequency response

Piezoelectric actuators are perfect for haptic applications as they can provide a wide range of frequencies. Piezo specifically engineered for haptic feedback can provide a frequency range from 1 Hz to 1 kHz.

All piezoelectric actuators have a natural frequency at which they resonate. This frequency is determined by the mechanical properties of the actuator, such as its mass and stiffness, as well as the electrical properties of the piezoelectric material. The important thing to note is that this frequency also depends on the load that the actuator is driving:

$$f_{res} = \frac{1}{2\pi} \sqrt{\frac{k}{m_{eff} + m_{load}}} \quad (3.1)$$

Where:

- f_{res} = Resonant frequency [Hz]
- k = Stiffness of the piezo actuator [N/m]
- m_{eff} = Effective mass of the actuator [kg]
- m_{load} = Mass of the load [kg]

As the frequency of the actuator approaches its resonant frequency, the amplitude of the actuator's motion increases significantly. This phenomenon must be taken into account when designing a control system for the piezo actuator, as at maximum voltage the actuator could be damaged if in resonance.

Force performances

Taking as an example a piezo actuator built specifically for haptic feedback, the PowerHap series from TDK [12], we can see that the actuator can provide a force up to 20N in a frequency range from 1 Hz to 500Hz.

Power consumption

Considering still as an example the PowerHap series from TDK, we can read from the datasheet that the actuator can be run with a peak voltage of 120V and an average current of 0.432A (calculated using [13] in the case of a square wave signal of 500Hz). This means that the actuator can consume up to 25.9 of power at its peak frequency. In the same condition, it will also dissipate about 2.59W of power as heat.

3.2.2 Texture rendering

- frequency requirements
- force requirements
- response time

Chapter 4

Powering circuit design

In this chapter, we will present some of the engineering challenges faced during the design of a power circuit for our flexible voice coil actuator. We will mostly describe an ideal circuit as we will later demonstrate that running this actuator would require very advanced analog circuitry, comprised of high-cost components. Most of the tests we will present have been done using a bench signal generator and amplifier.

4.1 Power Circuit Block diagram

To design the power circuit for the flexible voice coil actuator, we started by analyzing the requirements of the actuator. First of all, we want the coil to be driven with a sinusoidal AC signal at various frequencies and amplitudes; so the first component to consider it's the system's controller which in this case, can be a simple signal generator. For our application, we chose a simple ESP32 microcontroller, which has an integrated DAC.

Then we have to consider the power requirements to run the chosen coil. The impedance of a Flexar coil, as we discussed before, is in the order of 30Ω . The impedance of the coil is too low to be driven directly by the ESP32 DAC, so a power stage is needed. For the sake of simplicity, we chose to implement a power stage with a fixed gain of 10.

Then we want the amplitude of the signal to be adjustable, so we need a conditioning circuit to adjust the amplitude of the signal coming from the DAC before being amplified.

The control circuit can be summarized as a block diagram, as shown in figure 4.1.



FIGURE 4.1: Block diagram of the power circuit.

4.2 Controller

The controller in this application has to be a signal generator that can produce a waveform that can be amplified and sent to the coil. The controller we used for



FIGURE 4.2: ESP32 16Hz Sine wave generated by the ESP32 Signal Generator software.

testing is an ESP32 microcontroller. We chose this controller as the first test hardware for its simplicity of programming and its integrated DAC.

4.2.1 ESP32 DAC Characteristics

The DAC included in the ESP32 is a pretty basic one but as a first test, it is enough. The DAC has a resolution of 8 bits, and it can output a voltage between 0 and 3.3V with a maximum current output of 12mA.

4.2.2 ESP32 waveform generator

Using a simple program the ESP32 can be used as a pretty capable waveform generator. The software we used is the **ESP32 Signal Generator** from corz.org [1]. This software allows the user to generate the following waveforms:

- Sine wave from 16Hz to 500kHz
- Square wave from 1Hz to 40MHz
- Triangle wave from 153Hz to 150kHz
- Sawtooth wave from 153Hz to 150kHz

Between these ranges of frequencies, the generated waveforms are pretty accurate.

4.3 Signal Conditioning Circuit

We know that the controller DAC outputs a voltage between 0 and 3.3V, the power stage has a gain of 10, and that to drive Flexar's coils, at their rated maximum power of 0.8W, we need to provide a voltage of about 6V at a current of 0.2A.

A very simple solution is to implement a variable voltage divider to adjust the amplitude of the signal coming from the DAC. We chose a maximum dividing factor of 10 to match the power stage gain.

Where:

- V_{DAC} is the voltage coming from the controller DAC [0,3.3]V.

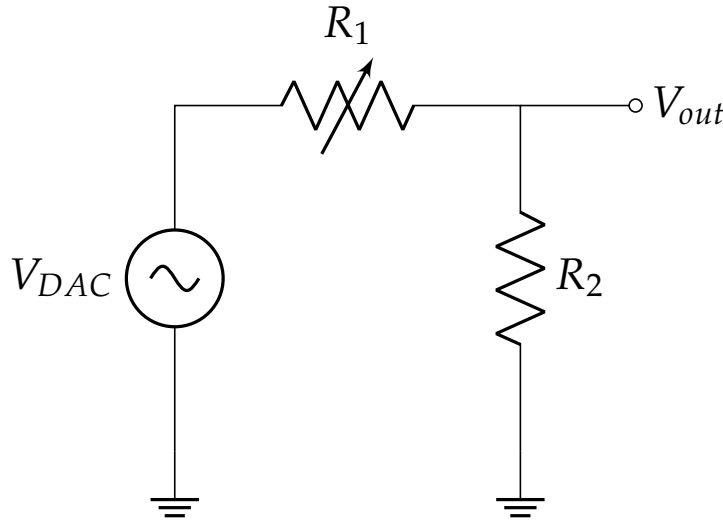


FIGURE 4.3: Signal conditioning circuit.

- R_1 is a $100k\Omega$ potentiometer to adjust the amplitude of the signal.
- R_2 is a $10k\Omega$ resistor to set the maximum amplitude of the signal.
- V_{out} is the output voltage of the conditioning circuit $[0, 0.33]\text{V}$.

The output voltage of the conditioning circuit is given by the following formula:

$$V_{out} = V_{DAC} \cdot \frac{R_1}{R_1 + R_2} \quad (4.1)$$

The values of R_1 and R_2 have been chosen to be $100k\Omega$ and $10k\Omega$ respectively, as they are standard values, provide a good range of adjustment for the amplitude of the signal, and their order is big enough to work with the provided DAC current of 12mA .

4.4 Amplifier circuit

As the Flexar's coil impedance is 30Ω , and the maximum power they can withstand is 0.8W , the power stage must be able to provide a voltage of about **6V** at a current of **0.2A**.

Such a high current requires the use of a power amplifier, usually an of the shelf audio amplifier could be used but such devices are built to handle only the audible frequency range (20Hz - 20kHz), and our actuators must be able to work between 1Hz and 1kHz which corresponds to the human tactile perception range.

A solution is to implement a custom amplifying circuit based on a special type of operational amplifier, the Power OP-AMP.

4.4.1 Power Operational Amplifiers

Power operational amplifiers (power op-amps) are a specialized class of operational amplifiers designed to handle higher current and power levels than standard op-amps. While traditional op-amps are primarily used for signal processing and conditioning in low-power applications, power op-amps are essential for driving heavy

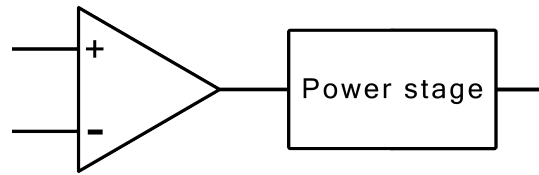


FIGURE 4.4: Power Op Amp block diagram.

loads, including motors, speakers, and other devices that require substantial power. Power op-amps integrate the fundamental principles of conventional op-amps—such as high gain, high input impedance, and low output impedance—with the ability to deliver higher current and power.

These devices are composed of simple op-amp circuits with a power stage, usually a power transistor, connected to the output of the op-amp. The power stage is responsible for delivering the required current to the load, while the op-amp provides the necessary voltage gain and feedback control.

Power op-amp characteristics

Any op-amp that can deliver more than 100mA of current is considered a power op-amp; there exist models that can deliver up to 10A. For our application, we chose a power op-amp that can deliver up to 1A of current, as it is more than enough to drive the Flexar's coils for simple AC signals. Another factor for this decision is the high cost of these components, especially at higher current ratings, due to their complexity and the scarcity of requests for this type of component from the market.

The component we landed on is the **L272** from STMicroelectronics, this small chip can deliver up to a sustained 1A of current, 1.5A of peak current, and can handle a maximum supply voltage of 28V.

In dynamic conditions is also to be noted that the L272 has a slew rate of $1 \frac{V}{\mu s}$ and, a gain-bandwidth product of 350kHz [7].

Power dissipation problems

A big problem with power op-amps is the power dissipation, as they are designed to deliver high current levels, they also dissipate a lot of power, which can lead to overheating and damage to the device.

For example, the L272 can handle up to 145°C but at only 5W it reaches 75°C, so a heat sink is required to keep the device at a safe temperature.

4.4.2 High Power Voltage Amplifier

As we specified before we decided to implement a power stage with a gain of 10, starting with the circuit of a simple inverting amplifier (the real gain is -10 but for the sake of our application a wave flipped by 180° is acceptable).

The gain can be calculated using the following formula:

$$A = \frac{V_{out}}{V_{in}} = -\frac{R_f}{R_1} \quad (4.2)$$

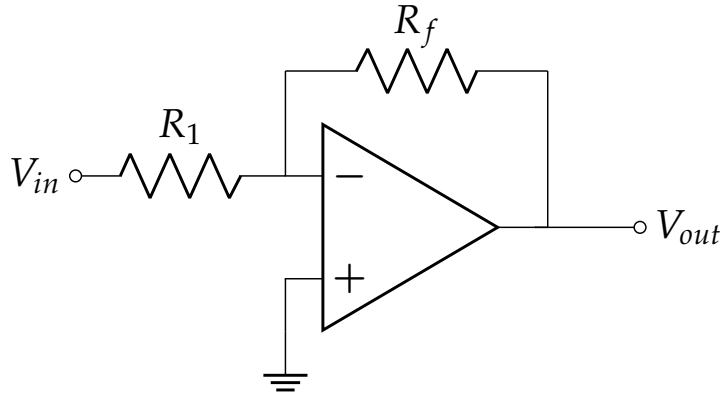


FIGURE 4.5: Inverting amplifier circuit.

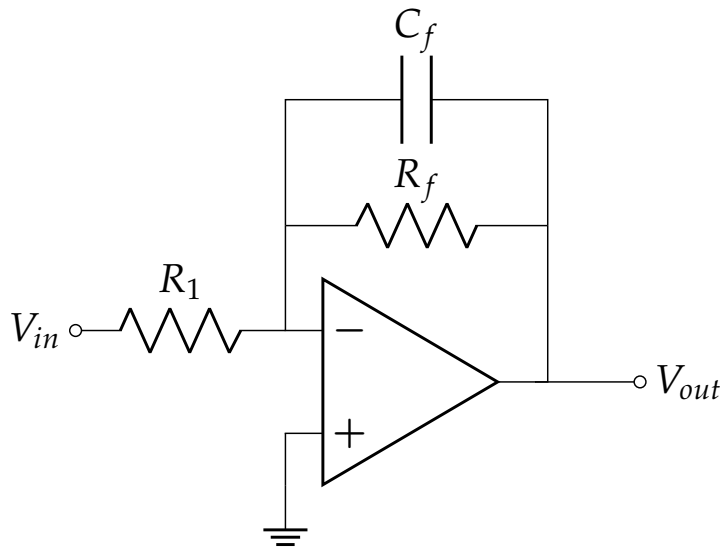


FIGURE 4.6: Inverting amplifier circuit with low-pass filter.

Where:

- V_{in} is the input voltage.
- V_{out} is the output voltage.
- R_1 is the input resistor.
- R_f is the feedback resistor.

The values of R_1 and R_f have been chosen to be $4.7k\Omega$ and $47k\Omega$ respectively, as they are standard values and their order is big enough to work with the provided DAC current of 12mA.

4.4.3 Noise filtering

While implementing the amplifier circuit, we noticed that the output signal had a lot of high-frequency noise, which was not present in the input signal.

To solve this problem, we decided to implement a simple low-pass filter adding a capacitor in parallel with the feedback resistor.

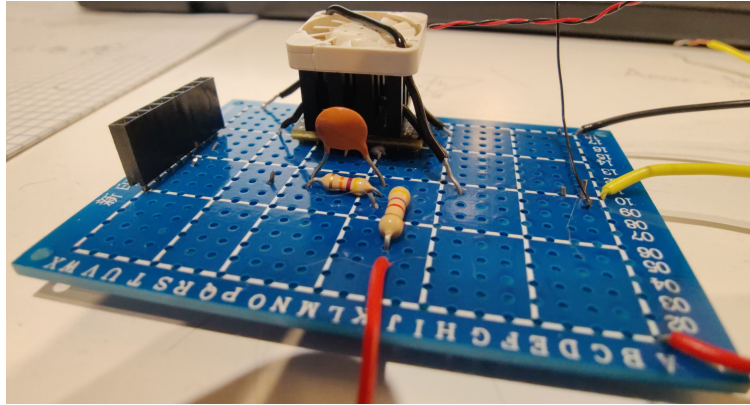


FIGURE 4.7: Picture of the implemented power stage.

The cutoff frequency of the filter can be calculated using the following formula:

$$f_c = \frac{1}{2\pi R_f C_f} \quad (4.3)$$

Where:

- f_c is the cutoff frequency.
- R_f is the feedback resistor.
- C_f is the capacitor in parallel with the feedback resistor.

We set a cutoff frequency of 50kHz, as it is high enough to filter out the noise but low enough to keep the signal intact. To achieve this, we chose a capacitor of 680pF, as it is a standard value and provides a cutoff frequency of 50kHz with the chosen feedback resistor.

Chapter 5

Implementation and Prototypes

5.1 Coils alternatives

This research was originally born from the willingness to explore the possibility of exploiting the technology of flexible coil inductors by using one produced by the research group Helmholtz-Zentrum Dresden-Rossendorf (HZDR) in Dresden, Germany [4]. After testing this coil, we realized its limitations and decided to explore other alternatives. For our research, we landed on Flexar coils, which as we discussed before are flexible PCB coils produced by the company microbots [8]. In this section, we will compare the Dresden coil with the Flexar coil, which is the one we chose to use in our research.

5.1.1 Dresda coils

Low magnetic field strenght

Fragility and low flexibility

Very high resistance and power needs

5.1.2 Flexar coils

Higher magnetic field strenght

Higher flexibility

Lower resistance and power needs

5.2 Rigid Prototypes

In conducting this research, careful consideration was given to the selection of tools and technologies that would best support the implementation, experimentation, and analysis processes. This section provides an overview of the programming languages, machine learning frameworks, data processing tools, and other technologies employed throughout the research.

5.2.1 1st version - Dresda Coils testbed

The primary programming language for this research was Python, chosen for its versatility, rich ecosystem, and widespread use in machine learning. Python's readability and extensive libraries facilitated efficient coding and experimentation.

Dresda Coils

Flexible magnetic membrane

Adjustable height platform for coil and membrane

5.2.2 Wearable Rigid Prototypes

Finger-Membrane interface

PyTorch is an open-source machine learning framework developed by Facebook's AI Research lab (FAIR). Its design philosophy emphasizes flexibility, enabling researchers and practitioners to tailor datasets and training procedures to specific requirements. The flexibility offered by PyTorch manifests in two key areas: custom datasets and custom training/validation phases. PyTorch supports automatic differentiation, making it easier to implement and experiment with complex neural network architectures. Its community, extensive documentation, and seamless integration with hardware accelerators like GPUs contribute to its popularity in both research and production.

PyTorch facilitates the creation of the custom dataset through the `torch.utils.data.Dataset` class.

By inheriting from this class and implementing the `__len__` and `__getitem__` methods, it's been possible to define datasets tailored to data structure and format used. This capability is invaluable when working with diverse data types, such as images or time-series, allowing seamless integration into PyTorch's data loading utilities.

PyTorch's flexibility extends to the training and validation phases, enabling users to define custom training loops, loss functions, and evaluation metrics. This is crucial for experimenting with novel architectures, incorporating domain-specific metrics, or implementing advanced training techniques. The ability to seamlessly integrate custom logic into the training process empowers researchers to push the b

Keep the distance from the coil

Heat dissipation

Pandas is a powerful data manipulation and analysis library for Python. It provides data structures like DataFrames that facilitate the handling of structured data. Pandas excels in data cleaning, manipulation, and exploration tasks, offering a plurality of functions for indexing, merging, grouping, and aggregating data. Its integration with other libraries, such as NumPy, makes it a go-to choice for working with labeled data and time series.

Pandas DataFrames offer a convenient and versatile way to handle tabular data, making them an excellent choice for storing and preprocessing data before creating datasets in PyTorch. The integration between Pandas and PyTorch simplifies the transition from data exploration to model training.

NumPy is a fundamental library for numerical operations in Python. It provides support for large, multi-dimensional arrays and matrices, along with an assortment of high-level mathematical functions to operate on these arrays.

Moreover, NumPy arrays and PyTorch tensors share several similarities, making them interchangeable in many contexts. These similarities contribute to a smooth

integration between the two libraries, facilitating data manipulation and interoperability.

The compatibility between NumPy and PyTorch simplifies data exchange and promotes a cohesive workflow in mixed-library environments.

Matplotlib is a versatile 2D plotting library for Python. Seaborn is a statistical data visualization library built on top of Matplotlib. It provides a high-level interface for creating attractive and informative statistical graphics. Seaborn simplifies the process of generating complex visualizations with concise syntax. It is particularly useful for exploring relationships in datasets through specific

5.3 Flexible Mat Prototypes

5.3.1 Design of the membrane

Material stiffness and thickness

Membrane structure vs magnet dimensions

5.3.2 Design of the mat

Distance magnet-coil

Coil trap

Production method and structure

5.3.3 Design faults and problems

Membrane fragility

Overall system flexibility

Keeping the distance coil-magnet under finger pressure

Production method

5.4 Experimentation and Evaluation

5.4.1 Heating testing

Single coil in DC

Single coil in AC [-V, V]

Single coil in AC [0, V]

Two coils in parallel DC

Two coils in parallel AC

5.4.2 Magnet size vs Force

5.4.3 Force vs number of coils

5.4.4 Voltage vs Force

Chapter 6

Discussion and conclusions

6.1 Challenges in On-Board AI Systems for Space Missions

AI algorithms in on-board space applications encounter significant challenges related to both verifiability and computational load, crucial factors for the success and safety of space missions.

6.1.1 Verifiability Issues

AI algorithms, particularly those employing deep learning, are characterized by intricate architectures and numerous parameters. The complexity of these models makes it challenging to provide comprehensive assurance of their correctness. In space applications, where system failures are not an option, ensuring the verifiability of AI algorithms becomes predominant.

Many AI models, including deep neural networks, lack inherent explainability. Understanding the decision-making process within these "black box" models is essential to verify their reliability. Achieving transparency in AI decision logic is critical in scenarios where the basis for decision-making must be interpretable, such as during critical space maneuvers.

Space environments are dynamic and may exhibit uncertainties. AI algorithms designed for adaptability and learning might introduce challenges in predicting their behavior accurately. Verifying the robustness of adaptive AI systems in the face of unforeseen conditions is a persistent concern.

6.1.2 Computational Issues

On-board space systems typically operate with limited computational resources due to factors such as size, weight, and power constraints (SWaP). Implementing AI algorithms with demanding computational requirements may strain available resources, affecting the overall efficiency of the system.

Certain space applications, such as autonomous navigation or hazard avoidance, demand real-time decision-making. AI algorithms with high computational loads may struggle to meet these stringent timing constraints. Delays in processing could lead to missed opportunities or, in critical situations, mission failure.

In addition to computational power, energy efficiency is a crucial consideration. Prolonged missions and the reliance on energy-harvesting sources necessitate AI algorithms that balance computational complexity with energy consumption, ensuring sustained and reliable operation.

Addressing these challenges requires a multidisciplinary approach involving AI researchers, space engineers, and mission planners. Techniques such as formal verification, explainable AI, and hardware optimization are essential to enhance the verifiability and efficiency of AI algorithms in on-board space applications.

6.2 Results Analysis

In the broader context, the multi-model configuration emerges as the more robust and adaptable option, showcasing superior performance on the test set and demonstrating effective generalization capabilities to previously unseen data. The overall system score on the test dataset is $S = 0.0447$, primarily affected by the translation component $S_T = 0.0390$, as opposed to the relatively lower contribution from the rotation aspect, $S_R = 0.0057$. The noteworthy aspect is the necessity of prioritize the minimization of translation errors, since, in proximity to the target, precise translation is crucial for accurate maneuvering. Moreover, rotation pose can be more effectively predicted with the incorporation of a navigation filter. This strategic integration allows for a corrective mechanism, compensating for rotational discrepancies and enhancing the system's overall precision in navigating close quarters.

6.3 Possible Improvements

Another option would be using multiple models also for the *Landmark Regression* module, which are able to identify a target set of landmarks in farther positions and a second set in closer distances to the target, in order to keep the number of identified points in the image frame as greater as possible.

This implementation would also lead to a more accurate pose estimation in positions closer to the minimum distance analyzed in the experiments (from 40cm to 20cm). A well-performed pose estimation in positions very close to the target would help to minimize any errors introduced by camera distortions.

6.3.1 Landmark Mapping Sensitivity

The assessment of trajectories such as *Less_Difficult_Trajectory* and *Difficult_Trajectory* is conducted with a noteworthy consideration: the assumption of zero prediction error for the points' location in the image. This assumption is made out of necessity since the *Landmark Regression* module encounters difficulties in identifying all the landmarks expected to be present in the image frames. Consequently, the input data for the *Landmark Mapping* module is marked by a heightened sensitivity, as the accuracy of its predictions is contingent upon the successful identification of landmarks by the preceding module.

A potential avenue for improvement involves an expansion of the training dataset to incorporate instances where certain landmarks remain unidentified due to inherent challenges in their recognition. This strategy aims to enhance the model's resilience to scenarios where specific landmarks pose persistent issues during identification. By exposing the model to a more diverse range of challenges and including cases of landmark ambiguity, it is anticipated that the trained model will develop a more robust understanding, leading to improved performance, particularly in situations mirroring real-world complexities. This adjustment aligns with the overarching goal of fortifying the system's adaptability and generalization capabilities, addressing

challenges posed by varying environmental conditions and unforeseen factors during autonomous space applications.

Moreover, to fortify the robustness of the system, there is a prospect to introduce a more sophisticated pre-processing system. This advanced system would be designed to mitigate the impact of varying image light conditions on landmark identification. By incorporating techniques such as adaptive image enhancement, contrast normalization, or even exploring deep learning-based methods for illumination invariance, the model could become less susceptible to fluctuations in lighting. Such enhancements would foster greater reliability in landmark identification by the *Landmark Regression* module, subsequently improving the overall accuracy of the *Landmark Mapping* module. This proactive approach anticipates and addresses challenges associated with real-world scenarios where illumination conditions can be unpredictable, ensuring the model's effectiveness across diverse operational environments in on-board space applications.

6.4 Conclusions

This project presents a dedicated monocular pose estimation framework designed for spaceborne objects, emphasizing its applicability to satellite rendezvous maneuvers. The framework capitalizes on the strengths of deep neural networks, seamlessly integrating feature learning and establishing robust 2D-3D correspondence mapping. Notably, the incorporation of HRNet, known for its high-resolution image representation, significantly contributes to the precision of pose predictions and the subsequent refinement process. The framework further demonstrates its efficiency by employing geometric optimization techniques, ensuring accurate alignment of point sets and enhancing the overall robustness of the pose estimation system.

Appendix A

Support Code

A.1 Ground Truth Heatmaps

```

1 import numpy as np
2
3 def createHeatmap(landmark, vp, hmap_w, hmap_h, sig=1):
4     hmap = np.zeros((hmap_height + 3, hmap_width + 3))
5     x, y = landmark
6     if vp:
7         for i in range(y - 3*sig, y + 3*sig):
8             for j in range(x - 3*sig, x + 3*sig):
9                 hmap[i,j] += np.exp(-((i-y)**2 + (j-x)**2)/(2*sig**2))
10
11     hmap = hmap[1:-2, 1:-2]
12
13     return hmap
14
15 def coord2Heatmap(landmarks, vis, hmap_w=512, hmap_h=512, sig=1):
16     hmaps = []
17
18     for landmark, vp in zip(landmarks, vis):
19         hmaps.append(createHeatmap(landmark, vp, hmap_w, hmap_h, sig))
20
21     hmaps = np.array(hmaps).squeeze()
22
23     return hmaps

```

LISTING A.1: Ground Truth Heatmaps

A.2 Landmark Location Selection

```

1 import numpy as np
2
3 def get_landmarks(landmarks_images, threshold1=-0.5, threshold2=-0.6):
4     landmarks2D = []
5     for img in landmarks_images:
6         Lnd_found = False
7         lndx = -1
8         lndy = -1
9         mask1 = img < threshold2
10        img[mask1] = -1
11
12        if np.max(img) > threshold1:
13            Lnd_found = True
14        elif np.max(img) > threshold2 and np.var(img) > 2e-6:
15            Lnd_found = True
16
17        if Lnd_found:
18            p_lndy, p_lndx = np.where(img == np.max(img))
19            lndx = np.round(np.mean(p_lndx))
20            lndy = np.round(np.mean(p_lndy))
21            if landmarks2D is not None or len(landmarks2D) > 0:
22                for data in landmarks2D:
23                    if data[2] == 1 and abs(lndx - data[0]) <= 3
24                       and abs(lndy - data[1]) <= 3:
25                        if np.max(img) > data[3] and np.var(img) > data[4]:
26                            data[0] = -1
27                            data[1] = -1
28                            data[2] = 0
29                            n_lnd = [lndx, lndy, 1, np.max(img), np.var(img)]
30                        else:
31                            n_lnd = [-1, -1, 0, np.max(img), np.var(img)]
32
33            n_lnd = [lndx, lndy, 1, np.max(img), np.var(img)]
34        else:
35            n_lnd = [-1, -1, 0, np.max(img), np.var(img)]
36
37        landmarks2D.append(n_lnd)
38
39    return np.array(landmarks2D)

```

LISTING A.2: Landmark Location Selection

Bibliography

- [1] corz.org. *ESP32 Signal Generator*. <https://corz.org/ESP32/square-sine-triangle-wave-signal-generator>.
- [2] Nicole D'Aurizio. "Algorithms and Wearable Technologies Enabling Haptic Communication". Available at <https://hdl.handle.net/11365/1225277>. PhD thesis. University of Siena, Jan. 2023.
- [3] Martin Geier et al. "Mathematical Modeling of an Electromagnetic Forming System with Flat Spiral Coils as Actuator". In: (Jan. 2010). DOI: 10.17877/DE290R-14276.
- [4] HZDR. *HZDR - Helmholtz-Zentrum Dresden-Rossendorf*. <https://www.hzdr.de>.
- [5] K. Kawabe, H. Koyama, and K. Shirae. "Planar inductor". In: *IEEE Transactions on Magnetics* 20.5 (1984), pp. 1804–1806. DOI: 10.1109/TMAG.1984.1063271.
- [6] A. Khurshid, Abdul Ghafoor, and Afzaal Malik. "Robotic Grasping and Fine Manipulation Using Soft Fingertip". In: Aug. 2011. ISBN: 978-953-307-373-6. DOI: 10.5772/23697.
- [7] L272: *Dual Power Operational Amplifier*. L272. STMicroelectronics. 2003. URL: <https://www.st.com/resource/en/datasheet/l272.pdf>.
- [8] microbots. *microbots Company*. <https://www.microbots.io>.
- [9] Minh Nguyen and Handy Blanchette. "Optimizing AC Resistance of Solid PCB Winding". In: *Electronics* 9 (May 2020), p. 875. DOI: 10.3390/electronics9050875.
- [10] Christian Østergaard et al. "Simulation and measurement of AC resistance for a high power planar inductor design". In: *2019 IEEE 13th International Conference on Compatibility, Power Electronics and Power Engineering (CPE-POWERENG)*. 2019, pp. 1–5. DOI: 10.1109/CPE.2019.8862361.
- [11] Stefano Papetti et al. "Vibrotactile Sensitivity in Active Touch: Effect of Pressing Force". In: *EEE Trans. Haptics* 10.1 (Jan. 2017), pp. 113–122. ISSN: 1939-1412. DOI: 10.1109/TOH.2016.2582485. URL: <https://doi.org/10.1109/TOH.2016.2582485>.
- [12] *Piezo Haptic Actuator - PowerHap*. PowerHap 15G. TDK. 2017. URL: https://www.mouser.com/datasheet/2/400/PowerHap_15G-1144538.pdf.
- [13] piezodrive.com. *Piezo Actuator Power Calculator*. <https://www.piezodrive.com/piezo-actuator-power-calculator/>.
- [14] supermagnete.de. *Magnetic field of various permanent magnets*. <https://www.supermagnete.de/eng/faq/How-do-you-calculate-the-magnetic-flux-density>.
- [15] The Engineering ToolBox. *Length of a Spiral*. https://www.engineeringtoolbox.com/spiral-length-d_2191.html [Accessed: 22/04/2024]. 2021.
- [16] John Wu et al. "Finite element analysis of the penetrations of shear and normal vibrations into the soft tissues in a fingertip". In: *Medical engineering & physics* 29 (July 2007), pp. 718–27. DOI: 10.1016/j.medengphy.2006.07.005.
- [17] Jonsenser Zhao. "A new calculation for designing multilayer planar spiral inductors". In: *Edn -Boston then Denver then Highlands Ranch Co-* 55 (July 2010), pp. 37–40.

Acknowledgements

Desidero esprimere i miei più sentiti ringraziamenti a tutte le persone che hanno contribuito al completamento di questa tesi.

Innanzitutto, desidero ringraziare il mio relatore, il prof. Marcello Chiaberge, e co-relatore, l'ing. Andrea Merlo, per avermi dato la possibilità di intraprendere questo progetto. Ringrazio l'ing. Marco Lapolla per la sua guida, disponibilità e dedizione nell'aiutarmi a sviluppare e perfezionare il mio lavoro.

Un ringraziamento speciale va alla mia famiglia che ha sempre sostenuto e incoraggiato il mio percorso accademico. Il loro sostegno e supporto sono stati la spinta necessaria per superare le sfide e raggiungere questo traguardo.

Ringrazio i compagni dell'università: Vale, Ali, Morgan, Matte, Nicoli, Franco, Luca e Nicco, che hanno alleviato le mie giornate e contro cui ho perso innumerevoli partite a bodriga.

Un ringraziamento agli amici di FORO, mia casa nell'ultimo periodo, con cui ho condiviso molte pause caffè.

Agli amici di una vita e compagni di mille avventure: Gian, Pier, Ale, Stol, Lollo e Chiara che, nonostante le nostre strade stiano prendendo direzioni diverse, sono e saranno sempre presenti al mio fianco.

Infine, il ringraziamento più importante va a Nau, mia compagna di viaggio, che mi ha sostenuto in questo percorso, credendo in me anche quando io non l'ho fatto.

Grazie mille a tutti.

Fede